CAMBRIDGE
UNIVERSITY PRESS

Article

Coexisting nanoscale phases of K-illite, NH$_4$,K-illite and NH$_4$-illite-smectite: an organic nitrogen contribution in the hydrothermal system of Harghita Bãi, East Carpathians, Romania

Iuliu Bobos*

Institute of Earth Sciences – Porto, Faculty of Science, University of Porto, Rua do Campo Alegre 687, 4168-007 Porto, Portugal

Abstract

Nitrogen influx was identified in the Harghita Bãi area, where the mechanism of NH$_4^+$-fixation in illitic clays is relevant for the N-input budget estimation. The nanotextural features of K-illite (K-I), NH$_4$,K-I and NH$_4$-illite-smectite (NH$_4$-I-S) mixed layers observed in argillic-altered andesitic rocks from the hydrothermal area of Harghita Bãi (East Carpathians) were studied by X-ray diffraction, infrared spectroscopy and transmission and analytical electron microscopy (TEM-AEM). The texture of undisturbed argillic-altered andesite rocks exhibits chaotic intergrowths of randomly oriented and curved illitic packets with abundant pore spaces and high porosity between packets. The TEM images of K-I and NH$_4$,K-I intergrowths show subparallel packets with clear contacts, exhibiting a diffuse contrast across layers. The thicknesses of K-I and NH$_4$,K-I packets range from 150 to 500 Å, and 1M_d and 1M polytypes were identified by selected area electron diffraction patterns. Crystal chemistry of K-I, NH$_4$,K-I and NH$_4$-I-S was carried out by AEM. A third interlayer cation Na$^+$ beside K$^+$ was detected in several NH$_4$,K-I packets. The NH$_4$,Na,K-I packets interleaved with NH$_4$,K-I or NH$_4$-I-S (12% smectite layers) packets were also identified by TEM. The thicknesses of NH$_4$,Na,K-I packets range from 300 to 1200 Å, with abundant lenses and lenticular layer separation along the boundaries between them. The 1M_d polytype dominates the NH$_4$,Na,K-I packets. Straight and parallel packets, continuous 00l layers and collapsed swelling layers at the boundary of individual NH$_4$-I (5% smectite layers) packets with thicknesses ranging from 20 to 95 Å were observed. The nanotextural observations indicate direct crystallization of NH$_4$-I crystals within a NH$_4$-I-S series from a pore fluid, where NH$_4$-I packets occupy void spaces previously occupied by fluids.

The geological cycle of nitrogen in the Earth system is slow, starting when organic matter sinks and settles in oceanic sediments. Once fixed in sediments and crust, N is converted to NH$_4^+$ via hydrolysis (Hall, 1999). Nitrogen may be carried into subduction zones, where it is volatilized (Elkins *et al.*, 2006), or carried into the mantle, where it is mostly recycled (Marty, 1995). Either subduction or volcanic–basement interaction zones with high geothermic gradients favour volatilization, where N as NH$_4^+$ may be incorporated in clay minerals from argillic envelopes (*i.e.* low- or high-sulfidation zones) related to the fossil hydrothermal systems (Bobos & Williams, 2017).

Because NH$_4^+$ has the same charge as K$^+$ and a similar ionic radius (1.43 Å and 1.38 Å, respectively), it may substitute K$^+$ in the mineral lattice sites; illite (I) is one of the minerals where the NH$_4^+$ may replace K$^+$, forming NH$_4$-I (Stevenson & Dhariwal, 1959; Higashi, 1982; Williams & Ferrell, 1991).

Several NH$_4$-I occurrences have been reported around the world in a wide variety of geological environments (*i.e.* sedimentary, metamorphic and hydrothermal). The structure, morphology, crystal chemistry and formation of NH$_4$-I in diagenetic to low-grade metamorphic shales, and anthracite-rank coal environments have been extensively studied by X-ray diffraction (XRD), infrared (IR) spectroscopy and electron microscopy techniques (Sterne *et al.*, 1982; Cooper & Evans, 1983; Juster *et al.*, 1987; Daniels & Altaner, 1990; Compton *et al.*, 1992; Lindgreen, 1994; Šucha *et al.*, 1994; Schroeder & McLain, 1998; Lindgreen *et al.*, 2000; Nieto, 2002; Drits *et al.*, 2002, 2005; Árkai *et al.*, 2004; Bauluz & Subías, 2010).

The NH$_4$-I samples in anthracite-rank coals described by Juster *et al.* (1987) were studied by Jiang *et al.* (1990a), where NH$_4$-I and K-I intergrown packets without smectite layers were identified by TEM. In very-low-grade metapelites from the Douro-Beira Carboniferous basin in Portugal, Nieto (2002) described the NH$_4$- and K-micas segregated into well-separated packets with few interstratifications. In addition, the NH$_4$-bearing mica layers intergrown with K-mica layers were identified in low-grade metaclastic rocks and polymetamorphic schists from the Betic Cordillera (Ruiz-Cruz & Sanz de Galdeano, 2008, 2010).

X-ray diffraction (XRD) is an accurate method for detecting the interstratifications between NH_4-I and other 2:1 layer types such as K-I, smectite or vermiculite (Drits *et al.*, 1997a). Thus, an I-S mixed-layer containing illite-tobelite-smectite and vermiculite interlayers was described previously (Drits *et al.*, 1997b, 2002, 2005; Lindgreen *et al.*, 2000), in which the layer thickness variations of interstratified layers significantly influenced the relationship between the basal reflection widths. Similarly, K-I and NH_4-I or K-I and paragonite mixed layers were also identified by XRD (Jiang & Peacor, 1993; Drits *et al.*, 1997a). However, the XRD technique is not sufficiently sensitive to identify heterogeneous I-S interstratified structures (Drits, 2003), requiring the application of the multi-specimen XRD method (Drits *et al.*, 1997b; Sakharov *et al.*, 1999).

Furthermore, the distribution of NH_4^+ and K^+ in the illite interlayer may be homogeneous or heterogeneous (Drits *et al.*, 1997a). Two different cases in relation to the NH_4^+ and K^+ distribution in the illite interlayer were assumed by Drits *et al.* (1997a, 2002, 2005): the K^+ and NH_4^+ were homogenously or rather heterogeneously distributed within each interlayer. The latter case represents a mixed-layer structure of K-I and NH_4-I layers and the former is similar to the formation mechanism of tobelite (NH_4-mica) described by Higashi (1978, 1982), in which a progressive substitution of K^+ for NH_4^+ was proposed.

The K-I and NH_4,K-I physical mixture and NH_4-I-S mixed layer with a percentage of smectitic layers (%S) ranging from 5% S to 40% S were identified in the hydrothermal area of Harghita Bãi from the Eastern Carpathians (Bobos, 2012; Bobos & Eberl, 2013). The structure, morphology and chemistry of the NH_4-I-S mixed layer (the <2 µm clay fractions) were studied to provide new insight into the mechanism of smectite tobelitization in hydrothermal systems (Bobos & Ghergari, 1999; Bobos, 2012). In addition, isotopic ($\delta^{18}O$; K–Ar) and trace rare earth element (*REE*) geochemistry was performed on the <2 µm clay fractions of the NH_4,K-I/K-I mixture and the NH_4-I-S mixed layer to constrain the timing of K-I (and NH_4-I) formation and the isotopic signature of NH_4-I crystallization (Clauer *et al.*, 2010).

The present study was largely built on previous work and aimed to examine the textural relationships of K-I, NH_4,K-I and NH_4-I-S (5%S or 12%S) as the important reservoir of N in silicate minerals. In addition, an understanding of the crystal chemistry of NH_4-I requires a more complete description of this mineral in order to determine the formation of NH_4-I in hydrothermal systems.

The NH_4-I-S samples with higher NH_4^+ contents reported in literature and NH_4-I with three interlayer cations (*i.e.* K^+ and Na^+) are studied at lattice scale by TEM-AEM. The main purpose of this work is to determine and to compare the textural, structural and crystal chemical characteristics of K-I, NH_4,K-I and NH_4-I-S mixed layers from undisturbed altered andesitic rocks.

Geological framework

The Neogene volcanism of the East Carpathians was related to the subduction of the East European Plate beneath the Tisza–Dacia continental microplate (Fig. 1a) (Seghedi *et al.*, 1998, 2004). The Cãlimani–Gurghiu–Harghita (CGH) volcanic chain (Fig. 1b), known for its diminishing age and volume southwards from 10 to 3.9 Ma, consists of calc-alkaline rocks that occurred along the easternmost margin of the rigid Tisza–Dacia block (Szakacs & Seghedi, 1995) and marks the end of the post-collisional subduction-related magmatism along the front of the

European convergent plate margin (Mason *et al.*, 1996, 1998; Seghedi *et al.*, 1998). The relatively large volume of magma in the CGH chain was associated with asthenosphere uprise, explained by progressive break-off of the Miocene subducted slab (Mason *et al.*, 1998; Seghedi *et al.*, 1998). Otherwise, Seghedi & Downes (2011) suggested only a post-collisional setting, where a large volume of calc-alkaline magmas was formed at destructive boundaries along transtensional faults (*e.g.* at margins of the Transylvanian basin).

The volcanic structure of the CGH volcanic chain consists of the eroded central-summit part of the volcanoes, including the generally unroofed intrusive core complexes and related hydrothermal alteration halos, the crater and/or caldera remnants that form the central facies (Szakacs & Seghedi, 1995). The anatomy of composite volcanic edifices comprises a proximal and distal facies with lava flows and pyroclastic interbeds.

The area north of the Harghita Mountains consisted of the complex volcanic structure of Vârghis–Harghita Bãi where the 'caldera' ('horseshoe depression') formation in the Vârghis region was formed by one or more edifice failures and debris avalanche events (Szakacs & Seghedi, 1995). An independent and partially buried smaller edifice occurs at the Harghita Bãi (southeast of the main summit), where an intrusive core complex and its eastern flank are visible. The andesitic rocks of the intermediate zone of the Vârghis–Harghita Bãi volcanic structure range in age from 5.3 to 4.1 Ma, Upper Pliocene, Pontian–Dacian (Peltz *et al.*, 1987).

The hydrothermal area of Harghita Bãi is the largest field of argillic alteration in the Neogene volcanic area of the Eastern Carpathians, where the magmatic–hydrothermal fluids generated an alteration halo (biotite → amphibole → propylitic → argillic) centred on the subvolcanic body, in which a possible porphyry copper system occurs (Stanciu, 1984).

K-I and NH_4,K-I clays (sample HB-9) were identified at –110 m outside of the breccia structure, whereas NH_4-I (samples HB-18 and HB-12) occurs in the barren part of the hydrothermal breccia structure. The breccia consists of irregular andesite blocks hydraulically fractured and argillized, where NH_4-I is the main clay mineral. The formation of NH_4-I was related to the post-breccia evolution.

Materials and methods

Materials

Samples were collected from the mine drafts and shafts located at –110 m (sample HB-9), –94 m (sample HB-18) and –80 m (sample HB-12) underground outside and within the hydrothermal breccias. The locations of samples across and around the breccia structure were shown by Bobos & Eberl (2013).

Two representative samples containing the NH_4-I-S mixed layer (samples HB-12 and HB-18) and one containing K-I + NH_4,K-I physical mixtures (sample HB-9) were selected for XRD, IR spectroscopy, scanning electron microscopy (SEM) and TEM. The <2 µm clay fractions of samples HB-9 and HB-12 had previously been studied for isotope and trace element geochemistry (Clauer *et al.*, 2010), sample HB-18 for structural, morphological and chemical studies (Bobos, 2012) and samples HB-9 and HB-18 for illite crystal thickness distribution (Bobos & Eberl, 2013).

Sample HB-12 was revisited because greater amounts of Na_2O than K_2O were measured in the <2 µm clay fractions by flame atomic absorption spectroscopy (see Supplementary Material,
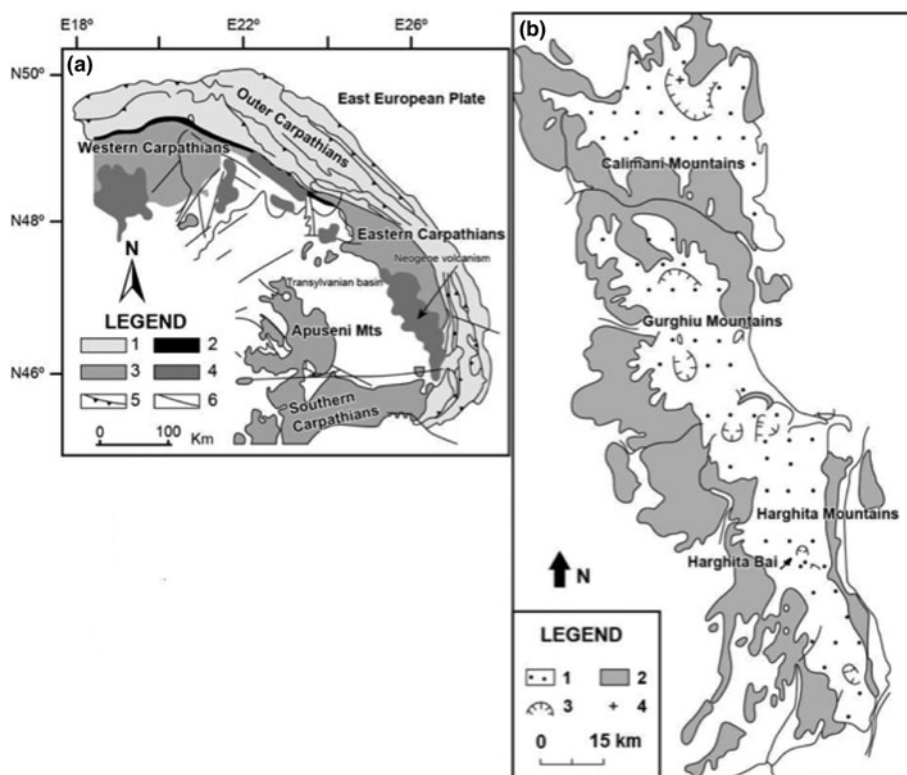
Fig. 1. (a) Geotectonic sketch of the Carpatho–Pannonian area showing major tectonic units and boundaries and the main occurrence areas of the Neogene calc-alkaline volcanic rocks from the East Carpathians (Seghedi *et al.*, 1998, 2004). Legend: 1 = Outer Carpathians (Moldavide), Neogene–Quaternary sediments and flysch nappes; 2 = Pieniny klippe belt; 3 = Pre-Neogene rocks of the inner Alpine–Carpathian Mountains; 4 = Neogene calc-alkaline volcanic areas; 5 = major thrusts; 6 = strike-slip faults. (b) Geological map of the Cǎlimani–Gurghiu–Harghita Mountains, where the central facies is constituted by enlarged central eroded volcanic depressions, the crater and/or caldera remnants and eruptive vents, whereas the proximal facies corresponds to lava flow piles and subordinate pyroclastic interbeds, which accompany the modified outer slopes of the volcanic edifices (Szakacs & Seghedi, 1995). Legend: 1 = upper structural compartment (central or 'core' and proximal or 'flank' facies model); 2 = lower structural compartment (peripheral distal or volcanoclastic facies model, which surrounds the bases of the volcanoes); 3 = craterial area; 4 = centres of eruptions.

available online) and related XRD patterns did not reveal a possible mixture with K-I. Sample HB-18 was selected due to a higher NH_4^+ content reported elsewhere (Bobos, 2012).

The andesitic samples with argillic alteration were crushed and sieved to a grain size of <177 μm. Then, the samples were chemically purified following the procedures described by Jackson (1975). Briefly, the samples were treated with Na-acetate (NaOAc) to remove carbonate (pH = 5.5; T = 100°C). Both Fe- and Al-oxyhydroxides were removed using Na-dithionite and Na-citrate (pH = 7; T = ~80°C). Excess salt was removed from the <2 μm clay fraction by dialysis using distilled water. The <2 μm clay fraction was separated by successive dispersion and sedimentation cycles in distilled water according to the Stokes' law. After extraction, the clay fractions were concentrated by centrifugation and re-dispersed with an ultrasonic probe.

Analytical techniques

X-ray diffraction
The oriented clay-aggregate specimens of the <2 μm fraction were prepared by clay suspension pipetting and drying onto glass slides. The XRD data were obtained in both an air-dried (AD) state and after ethylene glycol (EG) solvation with a Rigaku Giegerflex D/max C-series automated diffraction system (Institute of Earth Sciences, Porto, Portugal) using a graphite monochromator. Samples were analysed with Cu-Kα radiation in the range 2–50°2θ, using a 1° divergence slit, a step increment of 0.05°2θ and a counting time of 5 s/step.

The *NEWMOD©* computer program (Reynolds, 1985) enables estimation of the %S and verification of the NH_4-I-S structure behaviour based on the calculation of one-dimensional X-ray patterns. The data were acquired according to Moore & Reynolds (1997), where the maxima of the scattering amplitudes for K^+

and NH_4^+ were 18 and 10 electron units, respectively. Layer charge, total fixed cation content, hydration/swelling behaviour and 001 reflection values obtained from chemical and X-ray data were used to simulate the X-ray patterns. Calculations of XRD patterns for NH_4-I-S recorded were performed using three different configurations corresponding to the intercalation of zero, one or two water molecules in the smectite interlayer. This allowed the investigation of the NH_4-I-S mixed layer, where various hydration states coexist. The relative proportions of each mixed layer and of each layer type were adjusted to fit the experimental XRD patterns.

Infrared spectroscopy
15 mm discs were prepared by mixing 1 mg of sample (<2 μm fraction) with 200 mg of KBr and then pressing at 14 kg/cm². Prior to analysis, the pellets were heated overnight at 150°C to remove adsorbed water. The samples were studied in the absorption mode using a Bruker Tensor 27 spectrometer (Institute of Earth Sciences, Porto, Portugal) equipped with a deuterated triglycine sulfate single detector plate. The IR spectra were recorded in the 4000–400 cm^{-1} frequency region. The measurements of the integrated intensity of the vibration molecular bands were made with the *OPUS 4.2®* software supplied by Bruker.

Scanning electron microscopy
The rocks were crushed into small pieces (5–8 mm in diameter) and cleaned in an ultrasonic probe for SEM. The critical-point drying method was used (McHardy & Birnie, 1987) to preserve the textural morphology of clay minerals. The samples were mounted on a carbon holder and sputter-coated with a thin carbon film. The SEM study was performed with a Hitachi S-4100 electron microscope (DEMaC; University of Aveiro, Aveiro, Portugal) operated at an accelerating voltage of 25 kV and 5 nA

beam current, equipped with an X-ray energy-dispersive spectral spectrometer (Oxford Instruments INCA Energy). A 200 nm spot size and 100 s of live time were used.

Transmission and analytic electron microscopy

Representative areas identified by optical microscopy of the matrix of the altered andesites containing K-I and NH_4-I were selected from thin sections for TEM work. Very fine aggregated grains of NH_4-I observed in thin section showed distinguishing optical features characterized by the low birefringence light interference colour, which was different from the usual optical features of hydrothermal sericite.

Uncovered thin sections were prepared and copper rings with a single central hole of 1 mm in diameter were glued to the sections. Then, the rings plus sample were detached through gentle heating. Selected areas were further thinned with a Gatan Dual Ion Mill 600 using an acceleration voltage of 6 kV in three steps: (1) incident angle of 15° and probe current of 1 nA; (2) incidence angle of 12° and probe current of 0.6 nA; and (3) incidence angle of 12° and probe current of 0.4 nA. Selected areas were ion thinned following the procedure of Nieto (2002) and then carbon coated for TEM observations.

Two selected rings were taken from thin section of HB-9 (phyllic alteration and no brecciated rock sample) where three areas were labelled as specimens HB-9, HB-9a and HB-9a* for TEM-AEM investigation. Specimen HB-9 contains K-I and NH_4,K-I intergrowths, specimen HB-9a contains NH_4,K,Na-I and the specimen labelled HB-9a* contains NH_4,Na,K-I.

A Philips CM-20 scanning transmission electron microscope (STEM) fitted with an EDAX solid-state detector for energy-dispersive analysis was used (Centro de Instrumentación Científica, University of Granada, Granada, Spain). The TEM was operated at 200 kV with a point-to-point resolution of 2.7 Å in the TEM mode. The procedures suggested by Buseck (1992) and Buseck et al. (1988) were employed for the collection of TEM images and selected area electron diffraction (SAED) patterns.

Chemical analyses of the illite phases were made in STEM mode with an EDAX microanalysis system, where the quantitative chemical analyses were obtained only from thin edges. Areas for phyllosilicate analysis were selected on lattice-fringe images to control the textural position and to prevent contamination by other phases. The samples were tilted by 20° towards the detector. A 20 nm × 100 nm area, with the long axis oriented parallel to the phyllosilicate cleavage, was scanned using a 5 nm diameter beam. Albite, spessartine, muscovite, olivine, titanite and biotite were used to obtain K-factors for the determination of intensity ratios and concentration ratios (Cliff & Lorimer, 1975). Loss of alkalis (especially K^+) is a significant problem in the analysis of defect-rich minerals (Van der Pluijm et al., 1988); therefore, shorter counting times (30 s) were used as a compromise for K^+ measurements (Nieto et al., 1996). The concentration ratios were normalized to six cations in octahedral plus tetrahedral sites.

Results

X-ray diffraction

Sample HB-9 contains a physical mixture of K-I plus NH_4,K-I (Fig. 2a) in the <2 μm fractions. The XRD pattern of the K-I/ NH_4,K-I shows the 001 peak at 10.40 Å, which expanded after
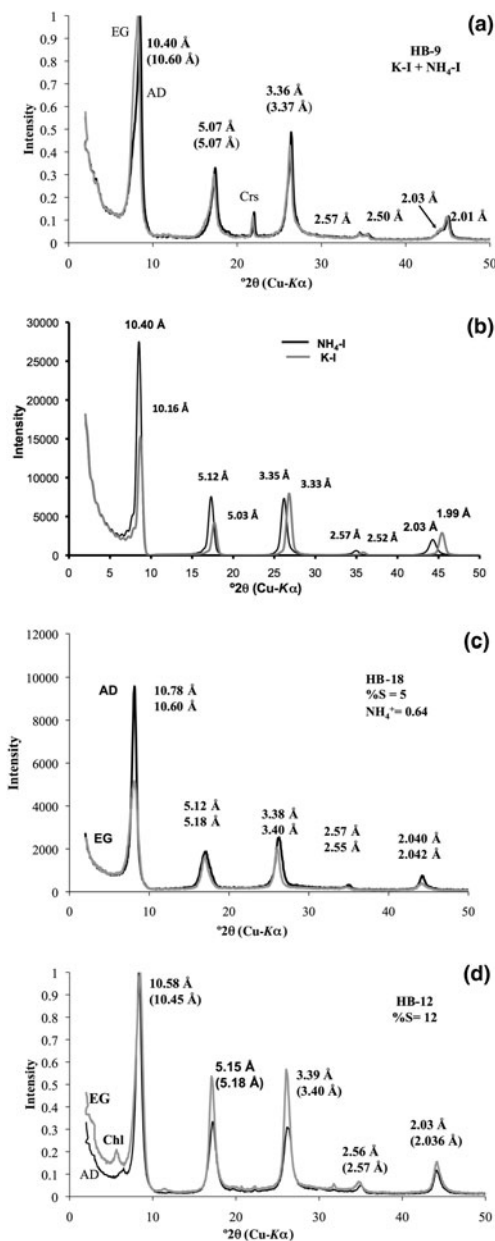
Fig. 2. (a) XRD patterns of the <2 μm clay fraction oriented specimens corresponding to NH_4,K-I/K-I mixed phase. (b) XRD patterns of NH_4-I and K-I were simulated (air-dried (AD) condition) using *NEWMOD©* code (Reynolds, 1985). XRD patterns of NH_4, K-I/K-I and NH_4-I-S mixed layers with (c) 5%S and (d) 12%S were obtained in AD (black lines) and ethylene glycol (EG) state (grey lines). XRD patterns in (a), (b) and (c) were adapted after Bobos & Eberl (2013). Chl = chlorite; Crs = cristobalite.

the EG solvation at 10.60 Å, suggesting a few smectite layers interstratified within NH_4,K-I (Fig. 2a). The intensity of the 001 peak of NH_4,K-I is greater than that of K-I, which indicates that the expandability observed is clearly related to NH_4,K-I. In addition, two distinct peaks are observed at 2.50 Å (K-I) and 2.57 Å (NH_4, K-I) for the 004 diffraction, whereas the 005 peak occurs at 2.00 Å (K-I), with a shoulder at 2.03 Å (NH_4,K-I) (Fig. 2a) that is well defined after the peak decomposition (see Supplementary Material).

The XRD patterns of K-I and NH_4,K-I were simulated (Fig. 2b) by mixing two calculated patterns of K-I plus NH_4-I (AD condition) and adding MIXER and MIX accessory data

files of *NEWMOD©* code (Reynolds, 1985). An assumption was that only NH_4^+ is fixed in NH_4-I interlayers and K^+ in K-I interlayers. The XRD patterns correspond to a mixed phase of NH_4-I and K-I in approximately equal proportions. The 001 peak of NH_4-I is higher than that of K-I in simulated XRD patterns of sample HB-9 (Fig. 2b). The 005 peak occurs at 2.06 Å (2.06 × 5.00 = 10.30 Å) for the end-member NH_4-I, which would mean that only NH_4^+ occurs in the interlayer site. In our case, the 005 peak at 2.03 Å corresponds to NH_4,K-I, and it was assumed that both NH_4^+ and K^+ cations are distributed homogeneously in each illite interlayer. The proportion of each mineral phase in sample HB-9 is 47% NH_4,K-I and 53% K-I according to the *UnMIXER* code (Eberl, 2002).

The samples HB-18 and HB-12 represent NH_4-I-S mixed layers with 5%S and 12%S, respectively. The XRD patterns of NH_4-I-S (Fig. 2c,d) correspond to a mixed layer with one-water layer smectite (sample HB-18) and two-water layer smectite (sample HB-12). The estimated %S and the number of H_2O molecules in the smectite interlayer were simulated from *NEWMOD* code (Reynolds, 1985). The %S estimated in sample HB-12 represents a mean value between 15%S and 10%S. The NH_4^+ and K^+ are homogeneously distributed in each illite interlayer corresponding to sample HB-18 (Bobos, 2012).

The 001 peaks of samples HB-9 and HB-12 were decomposed using the *MacDiff* code (Petschick, 2000). Two peaks were identified corresponding to K-I (10.03 Å) and NH_4,K-I (10.45 Å) for sample HB-9, and only one peak was identified at 10.45 Å in sample HB-12 (see Supplementary Material). There is no evidence of any paragonitic layers in the illite structure.

Infrared spectroscopy

Infrared spectra show values of absorption bands characteristic of illite minerals (Fig. 3). Four absorption bands attributed to N–H stretching and bending are observed at 3340 cm^{-1}, 3040 cm^{-1}, 2840 cm^{-1} and 1430 cm^{-1} (the bending band is at 1430 cm^{-1}). The absorption bands at 1430 cm^{-1} indicate the presence of NH_4^+ cations in illite, corresponding to the fundamental vibration (v_4) model for NH_4^+ (Chourabi & Fripiat, 1981; Nadeau & Bain, 1986; Petit *et al.*, 2006). Small amounts of quartz (815 cm^{-1} and 775 cm^{-1}) and cristobalite (796 cm^{-1} and 624 cm^{-1}) were identified in the HB-9 and HB-18 samples (Fig. 3).

Ammonium was quantified (samples HB-9, HB-18 and HB-12) using the areas of the OH^- stretching bands at 3640 cm^{-1} and the band vibration at 1430 cm^{-1}, being then transformed to optical intensities of I_{OH} and I_{NH4} (Higashi, 2000; Drits *et al.*, 2002). The NH_4^+ amounts estimated in illite crystals from the <2 μm clay
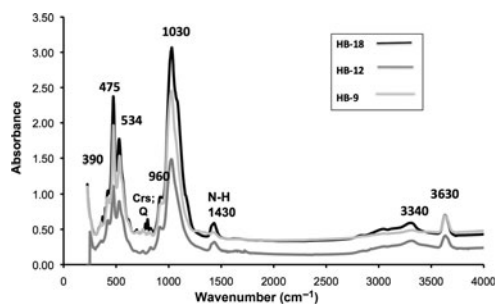
Fig. 3. IR spectra of NH_4,K-I + K-I (light grey line) and the NH_4-I-S mixed layer: samples HB-12 (grey line) and HB-18 (black line). N–H-bending vibration occurs at 1430 cm^{-1}. Crs = cristobalite; Q = quartz.

fractions are 0.60 atoms per formula unit (apfu; sample HB-18), 0.52 apfu (sample HB-12) and 0.43 apfu (sample HB-9).

Scanning electron microscopy

The illite minerals exhibit randomly oriented lath-like aggregates with variable widths in both HB-9 and HB-18 samples (Fig. 4). Two populations of illite aggregates with distinct morphologies were recognised in the HB-9 sample. Oriented crystals with a lath-shaped morphology and a smaller K^+ content correspond to NH_4-I (Fig. 4a). The other population attributed to K-I is composed of small pseudohexagonal platy aggregates (quadrangle area in Fig. 4a) and detailed platy aggregates (Fig. 4b). The lath-shaped crystals NH_4-I (5%S) are up to 2 μm long, also displaying a random orientation (Fig. 4c).

Transmission electron microscopy

Low-magnification TEM images (Fig. 5) were obtained on K-I/NH_4,K-I (sample HB-9) and NH_4-I-S mixed layers (samples HB-18 and HB-12), respectively. Sample HB-9 (Fig. 5a) exhibits randomly oriented NH_4,K-I/K-I packets with thicknesses estimated from 950 to 5000 Å. The TEM images (Fig. 5b,c) of NH_4-I-S (samples HB-18 and HB-12) show a texture composed of thin, randomly oriented packets with a size estimated from 350 to 1400 Å (sample HB-12) and from 300 to 700 Å (sample HB-18). In addition, a chaotic intergrowth of curved packets and abundant pore spaces occurs between packets (Fig. 5b,c).

#### Specimen HB-9: K-I and NH_4,K-I
Low-magnification TEM images show subparallel individual packets of K-I and NH_4,K-I exhibiting dark and light contrast, respectively (Fig. 6a). In addition, contrast is strongly observed along the NH_4,K-I packets. The interface between NH_4,K-I packets is defined by lines with light contrast or by sparingly abundant collapsed layers in the top left corner (Fig. 6a, labelled with small arrowheads). The thicknesses of NH_4,K-I packets range from 200 to 500 Å. In addition, slightly different orientations of illite packets are observed (Fig. 6a); namely, thin NH_4,K-I packets show a different orientation (arrow 2) from the subparallel packets of K-I and NH_4,K-I (arrow 1). The NH_4,K-I and K-I packets (Fig. 6a,b) were also analysed by AEM (Table 1). The SAED pattern of NH_4,K-I (Fig. 6a) corresponds to a one-layer polytype with abundant stacking disorder, where 001 reflections show a 10 Å periodicity.

Figure 6b shows K-I packets interleaved with a few NH_4,K-I packets. Variable degrees of curvature of K-I and NH_4,K-I packets and continuous lines with light contrast are observed (Fig. 6b, small arrowheads). K-I packets show fringes with 10 Å spacing (Fig. 6b), lattice distortion, high-strain fields (labelled with an asterisk) and few voids (labelled with a large arrowhead). Differences in contrast and spacings of lattice fringes (Fig. 6b) are typical of smectite-like layers within I-S sequences (Guthrie & Veblen, 1989; Veblen *et al.*, 1990). Lattice fringes are subparallel and discontinuous as a result of dehydration of smectite-like layers (quadrangle area, Fig. 6b). The SAED pattern shows a 1*M* polytype with a 10 Å periodicity for all 00*l* rows (Fig. 6b).

Specimens HB-9a* and HB-9a: NH_4,Na,K,-I and NH_4,K,Na-I
The NH_4,Na,K-I packets (Fig. 6c) correspond to specimen HB-9a* from the AEM data (Table 1), where the Na^+ content is greater than that of K^+. Low-magnification TEM images show a
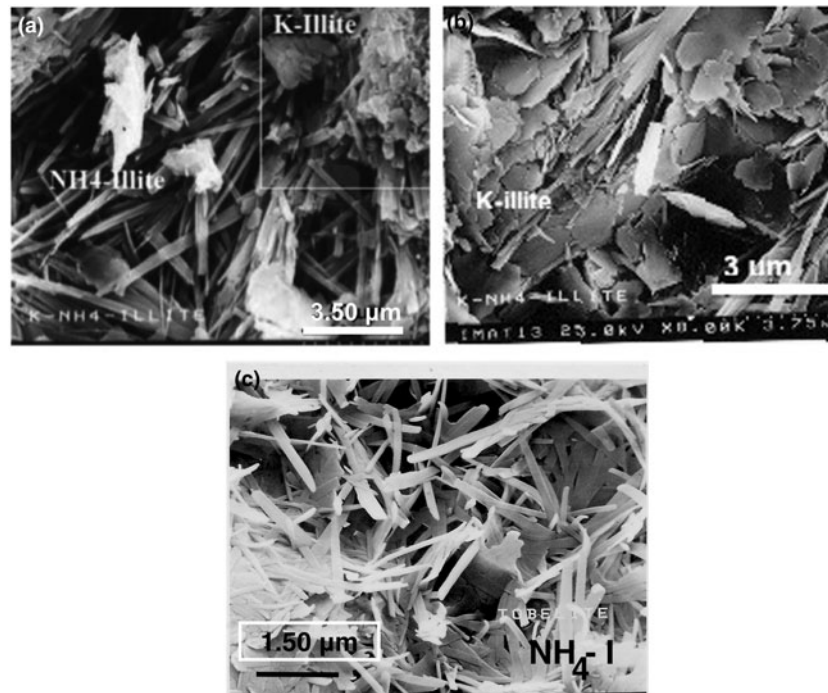
Fig. 4. SEM images of NH₄,K-I + K-I (sample HB-9) (a, b) and NH₄-I (sample HB-18) (c).

well-defined textural relationship between subparallel packets (Fig. 6c). The contrast is sharp between the packets of different illitic composition and well-defined boundaries occur between these packets. However, the pore spaces and lenticular layer separations (Fig. 6c, large arrowheads) occur along the boundaries between the NH$_4$,Na,K-I packets, where fissures along boundaries and thin lens or lenticular-layer separations are developed. Similar fissures and lenses observed in K-micas were attributed to electron-beam damage of paragonite layers (Ahn *et al.*, 1985; Jiang & Peacor, 1993). The widths of the lenses range between 60 and 240 Å, whereas the thicknesses of NH$_4$,Na,K-I packets range from 300 to 1200 Å.
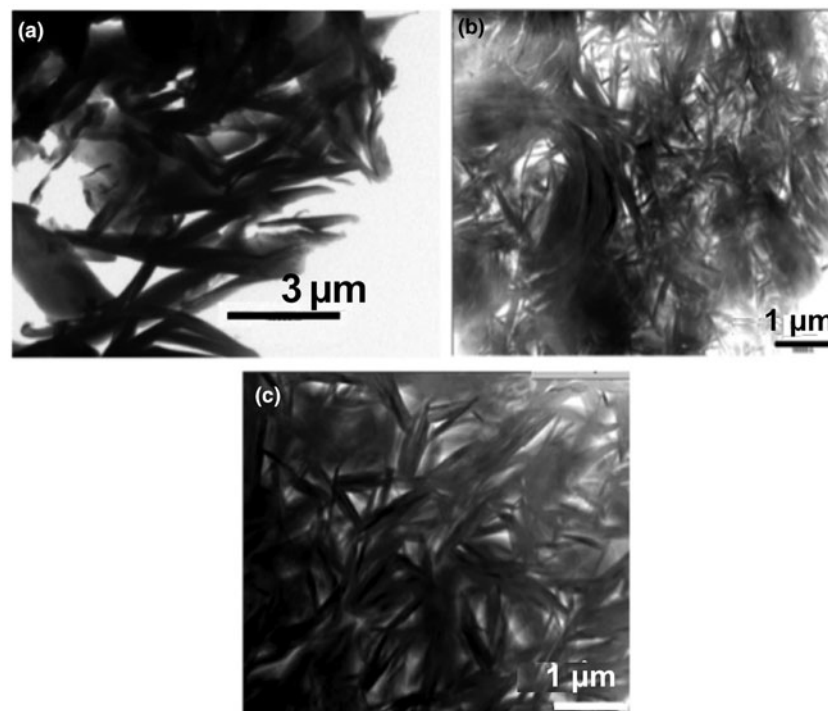
Fig. 5. Low-magnification TEM images showing an overview of NH₄,K-I + K-I (a) and the NH₄-I-S mixed layer with 5%S (b) and 12%S (c). Randomly oriented packets of NH₄,K-I/K-I (a) and a typical texture of 'tobelitic' rocks with chaotic intergrowths, open space pores and randomly thin oriented packets (b, c).
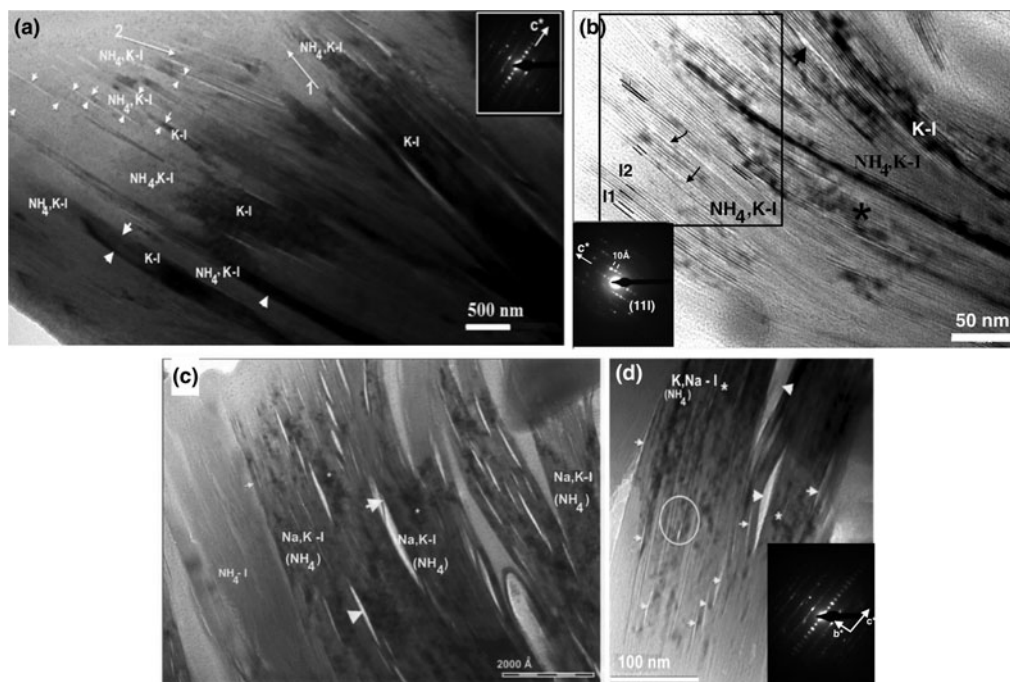
Fig. 6. (a) TEM image of subparallel K-I and NH$_4$,K-I packets (specimen HB-9) exhibiting dark and light contrast. Packets of illite with slightly different orientations are labelled with arrows 1 and 2. Collapsed smectite-like layers are indicated by the small arrowhead (left corner), whereas a net contact between packets is labelled with large arrowheads. The SAED pattern of NH$_4$,K-I shows a one-layer polytype with abundant stacking disorder. (b) TEM image of K-I (darker contrast) and NH$_4$,K-I interleaved packets. High-strain fields (marked with the asterisk) and narrow voids (labelled with the large arrowhead) are highlighted. Change in contrast of lattice fringes and differences in spacing of some NH$_4$,K-I layer sequences (quadrangle area) are typical of the presence of smectite-like layers where I-S individual units (I) are shown (I1 for 20–21 Å periodicity and I2 for ~31 Å periodicity). Lattice fringes in the NH$_4$,K-I packets are subparallel and discontinuous as a result of smectite-like layer dehydration (labelled with small arrowheads). The SAED pattern shows a $1M$ polytype. (c) TEM image showing NH$_4$,Na,K-I packet intergrowths (specimen HB-9a*) with straight interfaces parallel to basal planes. Lenticular pores or lens-like separation (labelled with arrowheads) occur along the basal planes between NH$_4$,Na,K-I packets, and high-strain fields (lattice distortion) are marked by an asterisk. (d) The NH$_4$,K,Na-I packets (specimen HB-9a) observed by TEM, where lenticular-layer separation (labelled with large arrowheads) and lattice fringes with structural imperfections at the fine scale corresponding to dislocation and different periodicity (labelled with a circle) are highlighted. Narrow voids are labelled with small arrowheads. The SAED pattern exhibits a $1M_d$ polytype.

The TEM images of NH$_4$,K,Na-I packets (specimen HB-9a) also show lenticular-layer separation (Fig. 6d, labelled with the large arrowheads) and lattice fringes with structural defects at the fine scale. Semi-coherent boundaries with defects in which the lattice fringes are mismatched were observed in NH$_4$,K,Na-I packets (labelled with a circle). The SAED pattern reflects disordered stacking sequences (Fig. 6d).

Sample HB-18: NH$_4$-I, 5%S
Lattice fringes show straight packets, sharp boundaries and continuous 00*l* layers (Fig. 7). Bright fringes of apparently collapsed smectite interlayers (labelled with small arrowheads) occur between the boundary of NH$_4$-I packets. Well-defined parallel packets formed by ~10 Å spacing layers often end abruptly by wedging out, becoming subparallel and thinner. Inclined interfaces to basal planes of NH$_4$-I associated with layer termination and low-angle boundaries between the crystallites (labelled with large arrowheads) are clearly observed. The thicknesses of NH$_4$-I packets range from 20 to 95 Å, with most being in the range of 30–70 Å.

The sequence of packets shows variable spacing and contrast, where some lattice fringes are uniformly darker than lighter adjacent ones. Parallel to subparallel packets with dark and light contrast exhibit either 20 or 10 Å spacing layers. The SAED patterns show 20 Å periodicity corresponding to the $2M_1$ polytype (Fig. 8a) or the one-layer polytype with abundant disordered stacking (Fig. 8b).

Sample HB-12: NH$_4$-I-S/NH$_4$,Na,K-I
Low-magnification TEM images of illite packets show chaotic orientation, open pore spaces, high porosity and differences in contrast that alternate from light to dark, where the lattice fringes of NH$_4$-I-S are interleaved with NH$_4$,Na,K-I packets (Fig. 9a). The low-magnification TEM image of a selected area with light contrast shows well-oriented NH$_4$-I-S packets with elongated voids along the boundary between packets (Fig. 9b). The lack of contrast between NH$_4$-I-S packets reflects the parallel to subparallel relative orientation of layers with a mean thickness of packets of ~40–45 Å. In addition, a few K-I layers (Fig. 9b, labelled with small arrowheads) show a difference in contrast from NH$_4$-I-S. The SAED pattern of the NH$_4$-I-S shows 00*l* diffraction spots corresponding to a $1M_d$ polytype (Fig. 9b, inset).

The contrast differences between NH$_4$-I-S and NH$_4$,K-I packets reflect their varying compositions. The packets with light contrast attributed to NH$_4$-I-S contain a very small amount of K$^+$ and presumably larger amounts of NH$_4^+$. The amounts of K$^+$ measured in various packets of sample HB-12 with dark and light contrast are shown in Fig. 10.

Analytic electron microscopy

The chemical compositions of K-I and NH$_4$,K-I (specimen HB-9), NH$_4$,Na,K-I (specimen HB-9a*) and NH$_4$,K,Na-I (specimen HB-9a) and NH$_4$-I-S mixed layers (samples HB-18 and HB-12) show large compositional variation (Tables 1, 2) in alkali elements.

Table 1. Crystal chemistry of K-illite and NH$_4$,K-illite (specimen HB-9), NH$_4$,Na,K-illite (specimen HB-9a*) and NH$_4$,K,Na-illite (specimen HB-9a) crystals analysed by analytic electron microscopy.

Sample	Si	Al^{IV}	Al^{VI}	Fe	Mg	Ca	K	Na	Al total	FM	Na/K	Na + K
HB-9	3.42	0.58	1.82	0.05	0.12	0.00	0.78	0.00	2.40	0.17	0.00	0.78
HB-9	3.36	0.64	1.96	0.04	0.00	0.00	0.69	0.00	2.60	0.04	0.00	0.69
HB-9	3.38	0.62	1.93	0.05	0.01	0.00	0.71	0.00	2.55	0.06	0.00	0.71
HB-9	3.35	0.65	1.82	0.08	0.10	0.00	0.63	0.00	2.47	0.18	0.00	0.63
HB-9	3.37	0.63	1.84	0.04	0.12	0.00	0.67	0.00	2.47	0.16	0.00	0.67
HB-9	3.39	0.61	1.81	0.03	0.15	0.00	0.24	0.00	2.42	0.18	0.00	0.24
HB-9	3.19	0.81	1.85	0.03	0.12	0.00	0.27	0.00	2.65	0.15	0.00	0.27
HB-9	3.33	0.67	1.86	0.07	0.07	0.00	0.36	0.00	2.54	0.14	0.00	0.36
HB-9a*	3.47	0.53	1.92	0.00	0.08	0.00	0.08	0.12	2.45	0.08	1.5	0.20
HB-9a*	3.30	0.70	1.91	0.03	0.05	0.09	0.05	0.38	2.62	0.08	7.60	0.43
HB-9a*	3.36	0.64	1.90	0.03	0.07	0.07	0.09	0.31	2.54	0.10	3.44	0.42
HB-9a*	3.38	0.62	1.95	0.02	0.03	0.03	0.07	0.41	2.56	0.05	5.86	0.48
HB-9a*	3.21	0.79	1.86	0.09	0.05	0.05	0.07	0.31	2.66	0.14	4.43	0.39
HB-9a*	3.12	0.88	1.74	0.17	0.09	0.03	0.05	0.24	2.63	0.26	4.8	0.29
HB-9a*	3.28	0.72	1.86	0.07	0.07	0.03	0.03	0.26	2.58	0.14	8.67	0.29
HB-9a*	3.34	0.66	1.88	0.08	0.04	0.02	0.04	0.28	2.68	0.12	7.00	0.32
HB-9a*	3.21	0.79	1.86	0.05	0.09	0.09	0.09	0.26	2.65	0.14	2.89	0.35
HB-9a*	3.47	0.53	1.90	0.03	0.07	0.00	0.14	0.22	2.43	0.10	1.57	0.36
HB-9a*	3.26	0.74	1.89	0.07	0.04	0.09	0.07	0.46	2.63	0.11	6.57	0.53
HB-9a	3.56	0.44	1.83	0.00	0.17	0.00	0.12	0.09	2.27	0.17	0.75	0.21
HB-9a	3.65	0.35	1.84	0.03	0.12	0.00	0.24	0.13	2.20	0.15	0.54	0.40
HB-9a	3.54	0.46	1.86	0.02	0.12	0.00	0.14	0.09	2.32	0.14	0.64	0.23
HB-9a	3.38	0.63	1.81	0.03	0.15	0.00	0.32	0.05	2.44	0.18	0.16	0.37
HB-9a	3.42	0.58	1.85	0.02	0.14	0.00	0.43	0.09	2.42	0.16	0.21	0.52
HB-9a	3.56	0.44	1.86	0.02	0.12	0.00	0.19	0.15	2.30	0.14	0.79	0.34
HB-9a	3.37	0.63	1.83	0.02	0.15	0.00	0.17	0.08	2.46	0.17	0.47	0.25
HB-9a	3.40	0.60	1.81	0.03	0.15	0.00	0.33	0.16	2.41	0.18	0.48	0.46
HB-9a	3.78	0.22	1.83	0.03	0.14	0.00	0.26	0.15	2.05	0.17	0.58	0.41
HB-9a	3.79	0.21	1.88	0.02	0.10	0.00	0.17	0.05	2.09	0.12	0.29	0.22
HB-9a	3.82	0.18	1.88	0.02	0.10	0.00	0.29	0.12	2.06	0.12	0.41	0.41
HB-9a	3.92	0.08	1.85	0.03	0.12	0.00	0.32	0.10	1.93	0.15	0.31	0.42

The mean value of NH$_4^+$ fixed in illite for the <2 μm fractions of NH$_4$-I-S in samples HB-18 and HB-12 is 0.60 apfu (Bobos, 2012) and 0.52 apfu (see Supplementary Material), respectively. In addition, the NH$_4^+$ estimated for the NH$_4$,K-I (sample HB-9) is ~0.43 apfu (Clauer *et al.*, 2010). The Na$^+$ and K$^+$ contents determined by flame photometry in the <2 μm clay fraction of NH$_4$-I-S (samples HB-18 and HB-12) and the K-I/NH$_4$,K-I mixture (Clauer *et al.*, 2010; Bobos, 2012) are comparable with the AEM data obtained in this study.

A synthesis of the results of the main structural (XRD plus SAED), morphological (SEM), textural (TEM) and chemical (mean values of Si, Al^{IV}, FM (Fe + Mg), K$^+$ and Na$^+$ determined

by AEM) characteristics of illite species described in this work is shown in Table 3.

Specimen HB-9: K-I and NH$_4$,K-I
Two populations of K-I (K$^+$ = 0.63–0.78 apfu) and NH$_4$,K-I (K$^+$ = 0.24–0.36 apfu) with variable compositions in alkali elements were identified in a single ion-milled sample (Fig. 6a,b). If we consider a total interlayer charge of 0.75/O$_{10}$(OH)$_2$ for a theoretical end-member NH$_4$-I (Drits *et al.*, 1997a), the NH$_4^+$ may range in NH$_4$,K-I packets from 0.39 to 0.51 apfu with a mean value of 0.45 apfu. This mean value was assumed after the recalculation of the structural formula including the NH$_4^+$ content estimated for the free interlayer space. Si ranges from 3.19 to 3.55 apfu with a mean value of 3.37 apfu in the NH$_4$,K-I packets, whereas
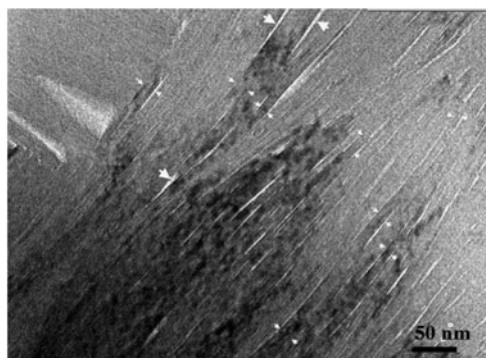
Fig. 7. TEM image of NH$_4$-I (5%S) packets (sample HB-18) showing straight interfaces parallel to the basal planes, where collapsed swelling layers (labelled with small arrowheads) occur at the boundary of individual packets together with low-angle boundaries between crystallites (labelled with big arrowheads).
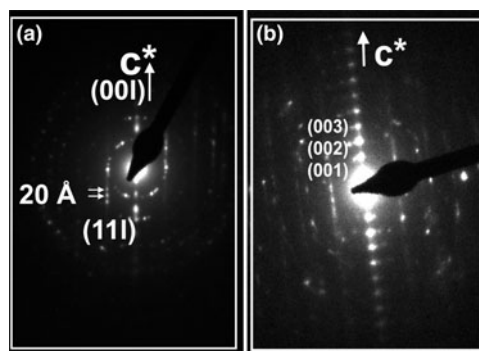
Fig. 8. SAED patterns corresponding to the (a) 2M_1 and (b) 1M_d polytype with stacking of disordered NH$_4$-I packets (sample HB-18).
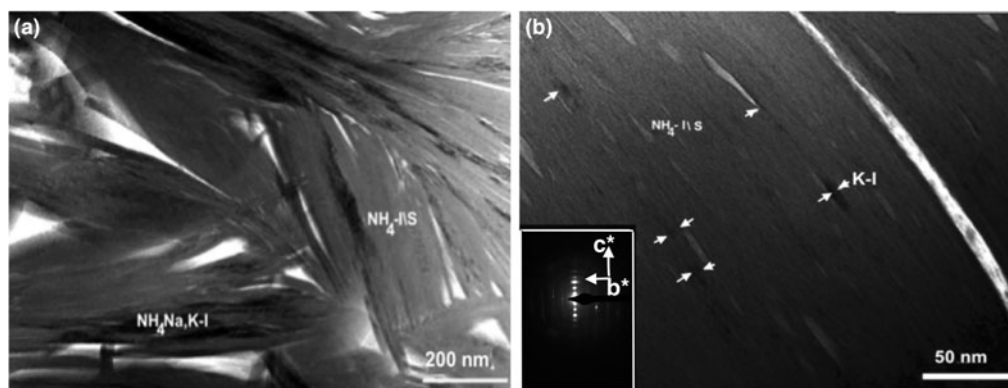
Fig. 9. (a) Low-magnification TEM image of NH_4-I-S and NH_4,Na,K-I packets (sample HB-12) showing chaotic orientation and open pore spaces. Textural relationship between NH_4-I-S and NH_4,Na,K-I packets is highlighted by light and dark contrast. (b) Low-magnification image of NH_4-I-S packets (sample HB-12) showing parallel to subparallel orientation of packets and elongated voids caused by NH_4^+ volatilization due to ion beam damage. A few K-I layers interstratified with NH_4-I-S are labelled with small arrowheads. The SAED pattern shows a $1M_d$ polytype.

the Al_{tot} ranges from 2.30 to 2.65 apfu (mean value: 2.48 apfu). Small amounts of Fe (∼0.03 apfu) and Mg (∼0.10 apfu) were identified in the NH_4,K-I packets.

Specimens HB-9a* and HB-9a: NH_4,Na,K-I and NH_4,K,Na-I

A greater Na^+ content than K^+ was measured in illite packets of specimen HB-9a* (Table 1). Si ranges from 3.12 to 3.82 apfu with a mean value of 3.47 apfu and the Al_{tot} from 2.20 to 2.65 apfu with a mean value of 2.43 apfu. A low Mg^{2+} content of 0.03–0.17 apfu was determined and Fe ranges between 0 and 0.17 apfu (mean value: 0.09 apfu), whereas the FM varies from 0.05 to 0.26 apfu (mean value: 0.16 apfu). The mean value of K^+ is 0.08 apfu, whereas the mean Na^+ value is 0.25 apfu. The sum of K plus Na ranges from 0.20 to 0.53 apfu with a mean value of 0.35 apfu. The estimated NH_4^+ content may range from 0.22 to 0.56 atoms/$O_{10}(OH)_2$ for NH_4,Na,K-I, with a mean value of 0.39 apfu. The existence of minor Ca^{2+} (0.02–0.07 apfu) is consistent with the presence of few smectite layers.

The NH_4,K,Na-I population containing more K^+ (mean value: 0.28 apfu) than Na^+ (Na^+ ranges from 0.05 to 0.16 apfu with a mean value of 0.11 apfu) was identified in specimen HB-9a (Table 1). Large amounts of Si (3.60 apfu) were detected, with the Al^{IV}/Si ratio (0.11) being smaller than that of the NH_4,Na,K-I sample. The mean value of Al_{tot} is 2.19 apfu, Fe is low (mean value: 0.02 apfu), Mg^{2+} ranges from 0.10 to 0.15 apfu and FM
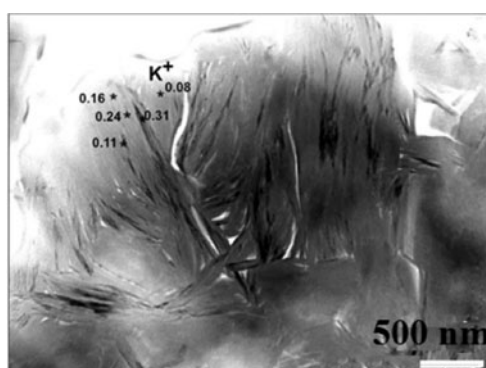
Fig. 10. Differences of contrast between packets of sample HB-12 and the variation in the K^+ content measured in several locations.

ranges from 0.12 to 0.18 apfu with a mean value of 0.15 apfu. This variation in alkalis and FM suggests a chemical disequilibrium.

Sample HB-18: NH_4-I, 5%S

A slightly greater amount of Si (mean value: 3.41 apfu) than the amount reported previously (3.35 apfu) was identified for the <2 μm clay fractions (Table 3). The mean value of Al_{tot} is 2.37 apfu, the Al^{IV}/Si ratio is 0.17 and K^+ is 0.15 apfu. The remaining site in the interlayer is compensated by NH_4^+ only. If the structural formula is recalculated by assuming the NH_4^+ cations fixed in the interlayer sites, the crystal chemistry obtained by AEM seems to be the same as the chemical composition previously reported for the <2 μm clay fractions (Bobos, 2012).

Sample HB-12: NH_4,Na,K-I and NH_4-I-S, 12%S

The mean value of Si is 3.55 apfu, the Al^{IV}/Si ratio is 0.12 and the Al_{tot} ranges from 1.97 to 2.46 apfu (mean value: 2.20 apfu). The Mg^{2+} content is 0.18 apfu and there is a small amount of Fe

Table 2. Crystal chemistry of NH_4-illite (sample HB-18) and NH_4,Na,K-illite (sample HB-12) crystals analysed by analytic electron microscopy.

	Si	Al^{IV}	Al^{VI}	Fe	Mg	Ca	K	Na	Al total	FM	Na/K	Na+K
HB-18	3.43	0.57	1.73	0.03	0.24	0.00	0.17	0.00	2.30	0.27	0.00	0.17
HB-18	3.43	0.57	1.80	0.05	0.15	0.00	0.14	0.00	2.37	0.20	0.00	0.14
HB-18	3.57	0.43	1.83	0.05	0.12	0.00	0.10	0.00	2.26	0.17	0.00	0.10
HB-18	3.50	0.50	1.83	0.02	0.15	0.00	0.07	0.00	2.33	0.17	0.00	0.07
HB-18	3.25	0.75	1.86	0.03	0.10	0.00	0.25	0.00	2.61	0.13	0.00	0.25
HB-18	3.38	0.62	1.83	0.03	0.14	0.00	0.12	0.00	2.45	0.17	0.00	0.12
HB-18	3.33	0.67	1.82	0.02	0.16	0.00	0.16	0.00	2.49	0.16	0.00	0.16
HB-18	3.41	0.59	1.84	0.05	0.11	0.00	0.08	0.00	2.34	0.16	0.00	0.08
HB-18	3.43	0.57	1.77	0.04	0.19	0.00	0.11	0.00	2.34	0.23	0.00	0.11
HB-18	3.46	0.54	1.77	0.02	0.21	0.00	0.15	0.00	2.31	0.23	0.00	0.15
HB-12	3.68	0.32	1.80	0.05	0.15	0.02	0.07	0.29	2.11	0.20	4.14	0.36
HB-12	3.59	0.41	1.80	0.03	0.17	0.02	0.05	0.12	2.20	0.20	2.40	0.17
HB-12	3.52	0.48	1.75	0.03	0.22	0.02	0.12	0.03	2.23	0.25	0.25	0.15
HB-12	3.35	0.65	1.75	0.03	0.22	0.00	0.03	0.15	2.39	0.25	5.00	0.18
HB-12	3.38	0.62	1.80	0.07	0.13	0.02	0.05	0.13	2.42	0.20	2.6	0.18
HB-12	3.75	0.25	1.71	0.03	0.25	0.02	0.03	0.16	1.97	0.28	5.33	0.19
HB-12	3.75	0.25	1.81	0.02	0.17	0.00	0.07	0.10	2.07	0.19	1.43	0.17
HB-12	3.76	0.24	1.80	0.02	0.19	0.00	0.05	0.22	2.04	0.21	4.40	0.27
HB-12	3.47	0.53	1.75	0.05	0.20	0.00	0.15	0.15	2.27	0.25	1.00	0.30
HB-12	3.72	0.28	1.81	0.03	0.15	0.02	0.07	0.18	2.09	0.18	2.57	0.27
HB-12	3.37	0.63	1.83	0.02	0.15	0.00	0.17	0.08	2.46	0.17	0.47	0.25

Table 3. The main structural (XRD + SAED), morphological (SEM), textural (TEM) and chemical (mean values of Si, Al^{IV}, FM (Fe + Mg), K$^+$ and Na$^+$ measured by AEM) characteristics of the samples analysed.

Samples	XRD (<2 μm fractions)	Specimens identified by TEM-AEM	SEM	TEM	SAED	AEM Si	Al^{IV}	Al^{IV}/Si	FM	K$^+$	Na$^+$	Na + K	Na$^+$/K$^+$	NH$_4^+$	Total interlayer cation
HB-9	K-I/NH$_4$,K-I (physical mixture)	HB-9	Platy	Intergrowth	1M	3.38	0.62	0.18	0.12	0.70	0.00	0.70	0.00	NA	0.70
		K-I	Lath shape	Intergrowth, pore spaces, fissures, thin lens and lenticular-layer separations along the boundaries	1M$_d$	3.37	0.63	0.19	0.12	0.30	0.00	0.30	0.00	NA	0.30
		NH$_4$,K-I HB-9a* NH$_4$,Na,K-I	–		1M$_d$	3.47	0.53	0.18	0.16	0.08	0.25	0.35	3.12	NA	0.35
		HB-9a NH$_4$,K,Na-I	–	Segregated domains (K$^+$, Na$^+$, NH$_4$)	1M$_d$	3.60	0.40	0.11	0.15	0.28	0.11	0.39	0.39	NA	0.39
HB-12	NH$_4$-I (12%S)	NH$_4$,Na,K-I	Lath shape	Parallel to subparallel orientation of packets with light contrast	1M$_d$	3.55	0.45	0.12	0.19	0.07	0.14	0.22	1.75	NA	0.22
HB-18	NH$_4$-I (5%S)	NH$_4$-I	Lath shape	Thick parallel NH$_4$-I packets with smectite interlayers at the boundary	1M$_d$ + 2M$_1$	3.42	0.58	0.17	0.19	0.15	0.00	0.15	0.00	NA	0.15

NA = not analysed.

(∼0.02 apfu), whereas the FM ranges from 0.17 to 0.28 apfu (mean value: ∼0.19 apfu). A greater amount of Na$^+$ (∼0.14 apfu) than K$^+$ (∼0.07 apfu) was detected in these packets. The Na plus K ranges from 0.15 to 0.36 apfu with a mean value of 0.22 apfu, and the Na/K ratio ranges from 0.25 to 5.53 (mean value: ∼1.75). The interlayer cation deficiency suggests the existence of variable amounts of interlayer vacancies filled in part by NH$_4^+$. The NH$_4^+$ content is estimated to range from 0.41 to 0.60 apfu, with a mean value of 0.53 apfu.

The amounts of fixed interlayer cations of the samples (HB-9, HB-12 and HB-18) were plotted in the ternary diagram of Na$^+$–K$^+$–NH$_4^+$ (Fig. 11). Five distinct fields were identified corresponding to K-I, K,NH$_4$-I, NH$_4$,K,Na-I, NH$_4$,Na,K-I and NH$_4$-I-S populations identified in the analysed samples.

## Discussion

Structural features

The XRD pattern of sample HB-9 confirms the presence in the <2 μm clay fractions of two distinct mineral phases: NH$_4$,K-I and K-I. The peaks at 2.50 Å (004 diffraction plane) and at 2.00 Å (005 diffraction plane) (Fig. 2a) correspond to K-I, whereas the 2.57 and 2.03 Å peaks correspond to NH$_4$,K-I or NH$_4$,Na,K-I packets identified by TEM-AEM, respectively. Theoretically, the interval ranging between 44 and 46°2θ would show the peak of K-I (100%) at 2 Å and that of 100% NH$_4$-I at 2.06 Å. The XRD pattern did not suggest the presence of a third possible interlayer cation, which in general is difficult to detect by powder XRD (Drits, 2003). Apparently, most of the Na$^+$ is included as a minor cation in the crystal structures of the other two phyllosilicates, and any real paragonitic domains, if they are present, are not sufficiently abundant to be detectable in the XRD traces.

The NH$_4$-I (5%S) contains a large amount of NH$_4^+$ cations fixed in the interlayer, as is also indicated by the 005 peak position at 2.04 Å. The sample HB-12 contains a mixture formed by NH$_4$-I-S (12%S) and NH$_4$,Na,K-I (Na$^+$ > K$^+$) identified in the TEM-AEM data (Table 2). Nevertheless, the XRD trace shows only a typical pattern of NH$_4$-I-S mixed layers (R3 with <15% S), in which the 005 peak at 2.03 Å suggests the presence of NH$_4$-I-S (NH$_4^+$ = 0.5 apfu) and NH$_4$,K-I, whereas the existence of the third component rich in Na$^+$ was not detectable as an independent mineral.

The NH$_4$-I-S samples may be considered equivalent to those described previously by Drits *et al.* (2005) as group II, in which K$^+$ and NH$_4^+$ are distributed homogeneously in each mica-like interlayer, and the structural varieties may have different contents of NH$_4^+$ and K$^+$. This was also shown for the NH$_4$-I-S series described by Bobos (2012). By contrast, the NH$_4$,K-I mixed layer might correspond to group I of Drits *et al.* (2005), in which 9.98 Å K-bearing and 10.33 Å NH$_4$-bearing layers contain either K$^+$ or NH$_4^+$. Interstratification of the layer type may be random or have some tendency for ordering. Nevertheless, the presence of Na$^+$ makes the samples different from those reported in the literature.

Nanotextural characteristics

The NH$_4$-I-S samples formed at a grade compatible with the persistence of small amounts of smectitic layers represent the first description at a lattice scale studied using TEM-AEM. The
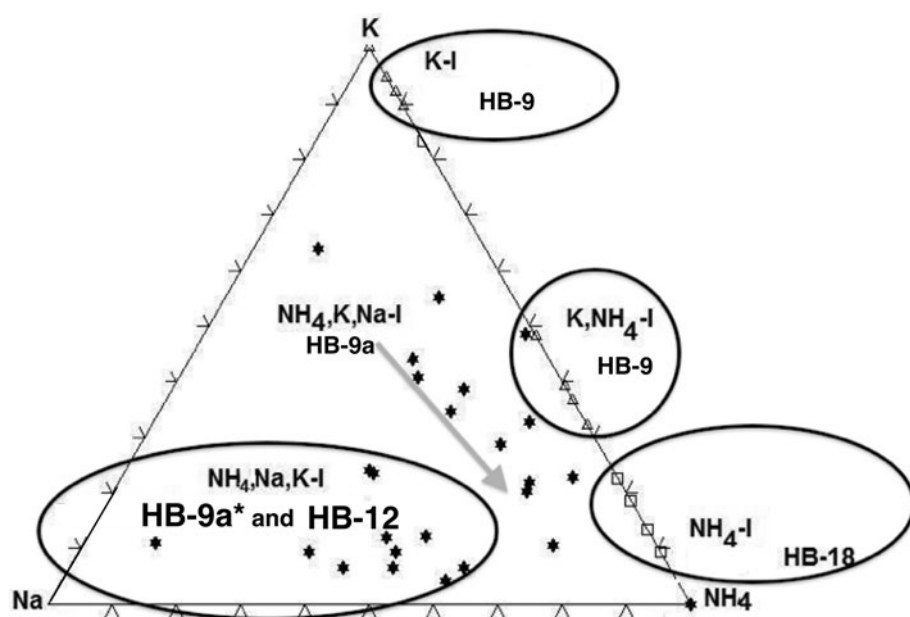
Fig. 11. The ternary diagram of K–Na–NH₄ showing the fields of K-I, NH₄,K-I, NH₄,K,Na-I, NH₄,Na,K-I and NH₄-I (5%S).

identification of samples containing both K-I and NH₄,K-I phases is also new in terms of the presence of NH₄,K-I packets in geological environments not linked to organic-rich sedimentary or low-grade metamorphic rocks. Finally, the presence of Na⁺ as a third major interlayer cation in the NH₄,K-I is also reported for the first time in the nanotextural study. The Na⁺ was only reported in the NH₄,Na,K-I packets by AEM, where Na–K or K–Na bulk composition may form domains in the interlayer sites (Livi *et al.*, 2008). The presence of Na-illite or brammallite (Bannister, 1942) was not detected in the XRD patterns.

Specimen HB-9 (K-I and NH₄,K-I) shows textural relationships (Fig. 6a) similar to the TEM images of Nieto (2002), where NH₄- and K-mica were identified as individual packets intergrown in very-low-grade metapelites. An unusual diffuse contrast feature is commonly observed along some elongated areas of NH₄,K-I packets with layers exhibiting gradual change in contrast across their length in the same packet. Otherwise, the alternating dark and light contrast of lattice fringes observed in Fig. 6a is typical of I-S minerals (Guthrie & Veblen, 1990; Veblen *et al.*, 1990; Bauluz, 2013). In addition, the K-I packets are well distinguished from the NH₄,K-I packets, where a diffuse contrast across the layers is observed (Fig. 6b). Furthermore, the SAED pattern of the NH₄,K-I shows the $1M_d$ polytype (Fig. 6a) or typical reflections for a $1M$ polytype (Fig. 6b).

The NH₄,Na,K-I packets (specimen HB-9a*) display lens-shaped voids or lenticular-layer separation between boundaries (Fig. 6c), showing a different textural relationship from the NH₄,K-I packets described previously. The areas associated with the high-strain fields may be attributed to the formation of fissures, lenses or lenticular layers owing to the different diffusion rates for K⁺ and Na⁺ (Ahn *et al.*, 1986). Lenses or lenticular-layer separation (which vary in size from a few tens to hundreds of ångstroms) may be produced by the heterogeneity induced by diffusion rates of cations, where higher mobility of Na⁺ is inferred compared to K⁺ in interlayer sites (Ahn *et al.*, 1986). The instability of NH₄,Na,K-I packets under electron beam relative to NH₄,K-I may be also related to Na⁺ and H₂O, besides NH₄⁺. The SAED pattern shows a single one-layer disordered polytype with one set of 00*l* reflections corresponding to ~10 Å periodicity (Fig. 6d).

Crystallization of the NH₄-I (sample HB-18) occurred in a permeable system (breccia structure) with a high-fluid water circulation and represents the end member from a NH₄-I-S series identified in the hydrothermal system of Harghita Bãi. Low-magnification TEM images of tobelitic rocks show a typical texture of open-space pores, suggesting direct crystallization of NH₄-I from a pore fluid, where NH₄-I-S packets occupy void spaces previously filled by fluids. In hydrothermal systems with a high water/rock ratio, dissolution occurs on a massive scale, with transport of dissolved components to distant sites where direct crystallization from solution may take place (Yau *et al.*, 1988).

The NH₄-I packets show thicknesses ranging from 50 to 70 Å with an average of ~60 Å. This value is in agreement with the values of 65–68 Å for the <2 µm clay fractions (sample HB-18) measured by Bobos & Eberl (2013). The NH₄-I (sample HB-18) consists of packets of relatively undeformed layers with fewer defects and smaller thicknesses, in which the packets occur either as separate particles or as stacks of particles with expandable interfaces (*i.e.* smectite interlayers). Various illitic packets are probably not always terminated by a smectitic interlayer due to the small proportion of smectite interlayers (5%) as measured by XRD. This scenario would produce packets formed of a large number of illitic layers. Hence, the domains separated by two smectitic layers in turn need to be internally separated into more than one illite crystalline domain showing differences of orientation.

The SAED pattern of NH₄-I in sample HB-18 (Fig. 8a) shows slightly streaked rows of reflections owing to the small crystallite size and volatilization of NH₄⁺. In addition, the 00*l* streaks showing the first three spots more intense in magnitude observed in SAED pattern (Fig. 8b) should be a characteristic of NH₄-I minerals (Nieto, 2002). Various polytype sequences of one- and two-layer stacking orders identified in this sample may also generate a periodic contrast between adjacent layers shown in TEM images (Jiang *et al.*, 1990b).

Overall, $1M_d$, $1M$ and $2M_1$ polytypes were identified in the studied samples for NH₄,K-I, NH₄,Na,K-I and NH₄-I-S, with each illite packet showing distinct textural relationships, chemical characteristics or sizes. The identification of the $1M_d$ polytype is the result of a disordered arrangement of the interlayer-stacking angle in a series

of successive layers as a consequence of interlayer stepwise changes (Chen & Wang, 2007; Nieto *et al.*, 2010). Accordingly, the two polytypes, 1*M* and 2*M*$_1$, coexist within the same domain as randomly faulted sequences, whereas the 1*M*$_d$ polytype results from the fine intergrowth of the various polytypes. Changes in stacking sequences are not accompanied by changes in composition, and polytypism varies not only between the grains, but also within individual grains (Baxter-Grubb *et al.*, 1991).

Synthetic tobelite samples analysed by the Rietveld method contain 1*M*, 2*M*$_1$ and 2*M*$_2$ polytypes (Harlov *et al.*, 2001) or 1*M*, 2*M*$_1$, 2*M*$_2$, 3*T* and 2*Or* polytypes (Pöter *et al.*, 2007; Watenphul *et al.*, 2009). Recently, Capitani *et al.* (2016) identified the 2*M*$_2$ polytype (alternating ±60° rotations of the tetrahedral–octahedral–tetrahedral layers) by SAED in a tobelite sample collected from sedimentary rocks of the Armorican sandstones, where numerous stacking faults parallel to the (001) plane were observed.

However, it is not clear whether the various polytypes identified by XRD studies exist as single crystals or are intergrown domains within one single crystal (Harlov *et al.*, 2001). In addition, experimental data reported by Drits & Zvyagina (2009) confirm only two main polytypes (*i.e.* 1*M* and 2*M*$_1$) in K-I, which seems not to be the case for NH$_4$-I.

Chemistry

The average compositions determined by AEM for the various specimens are in agreement with the chemical compositions of the <2 μm fractions (Bobos, 2012). Chemical data (Tables 1, 2) show that those compositions have, on average, very scattered values for all elements. The compositions of NH$_4$,K-I, NH$_4$,Na, K-I or NH$_4$,K,Na-I grains span a wide range. Various specimens of the same sample HB-9 (*i.e.* HB-9, HB-9a* and HB-9a) studied by TEM show systematic chemical differences (Table 3), which are not related to various crystallite sizes, various textural positions or various polytypes.

Initially, I-S (R0, R1) tends to have a larger FM content and a smaller Al^{IV}/Si ratio at the onset of the smectite illitization reaction, but near the final stages, crystals have a larger Al^{IV}/Si ratio and a smaller FM content in a prograde sequence regardless of their formation environment (Boles & Franks, 1979). This is also confirmed in the NH$_4$-I-S series (Bobos, 2012), where the Al^{IV}/Si ratio increased from 0.095 to 0.210 and FM decreased from 0.31 to 0.16 apfu.

The NH$_4$,Na,K-I (Na > K or K > Na) packets identified suggest different conditions of crystallization from those of NH$_4$-I-S (samples HB-18 and HB-12). The coexistence of the dioctahedral illite-like phases (K-I, NH$_4$,K-I, NH$_4$,Na,K-I with Na > K or K > Na) in sample HB-9 is a clear indication of non-equilibrium conditions (Árkai *et al.*, 2004). The fixed interlayer cation distribution in the ternary diagram of K–Na–NH$_4$ confirms the various chemical trends and mineralogical reactions in the crystallization of NH$_4$-I minerals (Fig. 11).

Small domains of paragonite, muscovite and tobelite layers were described by Árkai *et al.* (2004). The NH$_4^+$ has an ionic radius that is greater than those of K$^+$ and Na$^+$, and the differences in size render the coexistence of various cations in the same interlayer unstable due to structural incompatibilities produced by the different geometries necessary for each cation. The overall model of interlayer cation distribution is compatible with the existence of solvus relationships due to the significant differences in size among the three cations, where the size of the solvus decreases with increasing temperature.

A new model characterized by an intermediate step of homogeneous composition to paragonite formation called the disordered compositionally intermediate was proposed by Livi *et al.* (2008), where the paragonite formation would involve some exsolution and/or recrystallization at high temperature. This model was based on the lattice-fringe image of mixed paragonite/muscovite crystals exhibiting domain structures (Livi *et al.*, 1997; see also: Shau *et al.*, 1991; Jiang & Peacor, 1993; Li *et al.*, 1994; Giorgetti *et al.*, 2000; Árkai *et al.*, 2004).

Conclusion

Illite clays from the Harghita Bãi hydrothermal area contain a large proportion of organic N as NH$_4^+$ and serve as tracers of the mobility of organic–sedimentary components from the upper continental crust. Nitrogen from various organic sediments from the volcano–basement interaction was transferred into the volcanic continental arc, reflecting a complete palaeo-biogeochemical cycle. The NH$_4^+$ fixation in illitic clays is useful in estimating the N input fluxes based on knowledge of the rates of NH$_4^+$ retained in illitic clays, where the fraction of N fixed in illitic clays is likely to be greater than in other hydrothermal areas where NH$_4^+$ was detected.

The samples studied show various textural relationships and structural and chemical differences, suggesting various fluid compositions and multiple events or time-dependent hydrothermal events. Segregation of immiscible NH$_4^+$, K$^+$ and Na$^+$ cations is interpreted as probably being due to 'nanodomains' in the illite packets. In fact, the presence of 'nanodomains' suggests that NH$_4^+$ and K$^+$ or even Na$^+$ cations might randomly coexist in the illite interlayer structure, where a 1*M*$_d$ polytype characterizes the NH$_4$,K,Na-I and NH$_4$,K-I packets.

The TEM observations of NH$_4$-I-S show stacks of particles that contain NH$_4$-I, with collapsed layers interpreted as smectite interlayers, where a prograde sequence from 1*M*$_d$ to 1*M* and 2*M*$_1$ polytypes may be assumed. A large amount of NH$_4^+$ was fixed in a new illite structure, where dissolution–crystallization is a dominant mechanism for the NH$_4$-I-S clays that operated at a variety of scales in a saturated water system.

References

Ahn J.H., Peacor D.R. & Essene E.J. (1985) Coexisting paragonite-phengite in blueschist eclogite: a TEM study. *American Mineralogist*, **70**, 1193–1204.
Ahn J.H., Peacor D.R. & Essene E.J. (1986) Cation-diffusion-induced characteristic beam damage in transmission electron microscope images of micas. *Ultramicroscopy*, **19**, 375–382.

Árkai P., Livi K.J.T., Frey M., Brukner-Wein A. & Sajgo C. (2004) White micas with mixed interlayer occupancy: a possible cause of pitfalls in applying illite Kübler index ('crystallinity') for the determination of metamorphic grade. *European Journal of Mineralogy*, 16, 469–482.

Bannister F.A. (1942) Brammallite (sodium-illite), a new mineral from Llandebie, South Wales. *Mineralogical Magazine*, 26, 304–307.

Bauluz B. (2013) Clays in low-temperature environments. Pp. 181–216 in: *Minerals at the Nanoscale* (F. Nieto & K.J. Livi, editors), EMU Notes in Mineralogy, 14. European Mineralogical Union, Mineralogical Society of Great Britain & Ireland, London, UK.

Bauluz B. & Subías I. (2010) Coexistence of pyrophyllite, I/S, R1 and NH_4^+-rich illite in Silurian black shales (Sierra de Albarracín, NE Spain): metamorphic *vs.* hydrothermal origin. *Clay Minerals*, 45, 383–392.

Baxter-Grubb S.M., Peacor D.R. & Jiang W.-T. (1991) Transmission electron microscope observations of illite polytypism. *Clays and Clay Minerals*, 39, 540–550.

Bobos I. (2012) Characterization of smectite to NH_4-illite conversion series in the fossil hydrothermal system of Harghita Bãi, East Carpathians, Romania. *American Mineralogist*, 97, 962–982.

Bobos I. & Ghergari L. (1999) Conversion of smectite to ammonium illite in the hydrothermal system of Harghita Bãi, Romania: SEM and TEM investigations. *Geologica Carpathica*, 50, 379–387.

Bobos I. & Eberl D.D. (2013) Thickness distributions and evolution of growth mechanisms of NH_4-illite from the fossil hydrothermal system of Harghita Bãi, eastern Carpathians, Romania. *Clays and Clay Minerals*, 61, 375–391.

Bobos I. & Williams L.B. (2017) Boron, lithium and nitrogen isotope geochemistry of NH_4-illite clays in the fossil hydrothermal system of Harghita Bãi, East Carpathians, Romania. *Chemical Geology*, 473, 22–39.

Boles J.R. & Franks S.G. (1979) Clay diagenesis in Wilcox sandstones of southwest Texas: implications of smectite diagenesis on sandstone cementation. *Journal of Sedimentary Petrology*, 49, 55–70.

Buseck P.R. (1992) Principles of transmission electron microscopy. Pp. 1–35 in: *Minerals and Reactions at the Atomic Scale: Transmission Electron Microscopy* (P.R. Buseck, editor), Reviews in Mineralogy, 27. Mineralogical Society of America, Washington, DC, USA.

Buseck P.R., Cowley J.M. & Eyring L. (1988) *High-Resolution Transmission Electron Microscopy and Associated Techniques*. Oxford University Press, Oxford, UK.

Capitani G.C., Schingaro E., Lacalamita M., Mesto E. & Scordari F. (2016) Structural anomalies in tobelite-$2M_2$ explained by high resolution and analytical electron microscopy. *Mineralogical Magazine*, 80, 143–156.

Chen T. & Wang H.J. (2007) Determination of layer stacking microstructures and interlayer transition of illite polytypes by high-resolution transmission electron microscopy (HRTEM). *American Mineralogist*, 92, 926–932.

Chourabi B. & Fripiat J.J. (1981) Determinations of tetrahedral substitutions and interlayer surface heterogeneity from vibrational spectra of ammonium in smectites. *Clays and Clay Minerals*, 29, 260–268.

Clauer N., Liewig N. & Bobos I. (2010) K-Ar, $\delta^{18}O$ and *REE* constraints to the genesis of ammonium-illite from Harghita Bãi hydrothermal system, Romania. *Clay Minerals*, 45, 393–411.

Cliff G. & Lorimer G.W. (1975) The quantitative analysis of thin specimens. *Journal Microscopy*, 103, 203–207.

Compton J.S., Williams L.B. & Ferrell Jr R.E. (1992) Mineralisation of organogenic ammonium in the Monterey Formation, Santa Maria and San Joaquin basins, California, U.S.A. *Geochimica et Cosmochimica Acta*, 56, 1979–1991.

Cooper J.E. & Evans W.S. (1983) Ammonium-nitrogen in Green River Formation oil shale. *Science*, 219, 492–493.

Daniels E.J. & Altaner S.P. (1990) Clay mineral authigenesis in coal and shale from the Anthracite region, Pennsylvania. *American Mineralogist*, 75, 103–111.

Drits V.A. (2003) Structural and chemical heterogeneity of clay minerals. *Clay Minerals*, 38, 403–432.

Drits V.A., Lindgreen H. & Salyn A. (1997a) Determination of the content and distribution of fixed ammonium in illite smectite by X-ray diffraction: application to North Sea illite-smectite. *American Mineralogist*, 82, 79–87.

Drits V.A., Sakharov B.A., Lindgreen H. & Salyn A. (1997b) Sequential structural transformation of illite-smectite-vermiculite during diagenesis of Upper Jurassic shales from North Sea and Denmark. *Clay Minerals*, 32, 351–372.

Drits V.A., Lindgreen H., Sakharov B.A., Jakobsen H.J., Salyn A. & Dainyak L.G. (2002) Tobelitization of smectite during oil generation in oil source shales. Application to North Sea illite-tobelite-smectite-vermiculite. *Clays and Clay Minerals*, 50, 82–98.

Drits V.A., Sakharov B., Salyn A.L. & Lindgreen H. (2005) Determination of the content and distribution of fixed ammonium in illite-smectite using a modified X-ray diffraction technique: application to oil source rocks of western Greenland. *American Mineralogist*, 90, 71–84.

Drits V.A. & Zvyagina B.B. (2009) *Trans*-vacant and *cis*-vacant 2:1 layer silicates: structural feature, identification, and occurrence. *Clays and Clay Minerals*, 57, 405–415.

Eberl D.D. (2002) Determination of illite crystallite thickness distributions using X-ray diffraction, and the relation of the thickness to crystal growth mechanisms using MUDMASTER, GALOPER, and associated computer programs. Pp. 131–142 in: *Teaching Clay Science* (A. Rule & S. Guggenheim, editors). CMS Workshop Lectures, 11, The Clay Minerals Society, Aurora, CO, USA.

Elkins L., Fischer T., Hilton D., Sharp Z., McKnight S. & Walker J. (2006) Tracing nitrogen in volcanic and geothermal volatiles from the Nicaragua volcanic front. *Geochimica et Cosmochimica Acta*, 70, 5213–5235.

Giorgetti G., Tropper P., Essene E.J. & Peacor D.R. (2000) Characterization of non-equilibrium and equilibrium occurrences of paragonite/muscovite intergrowths in an eclogite from the Sesia–Lanzo Zone (Western Alps, Italy) *Contribution to Mineralogy and Petrology*, 138, 326–336.

Guthrie G.D. & Veblen D.R. (1989) High-resolution transmission electron microscopy of mixed-layer illite-smectite: computer simulation. *Clays and Clay Minerals*, 37, 1–11.

Guthrie G.D. & Veblen D.R. (1990) Interpreting one-dimensional high-resolution transmission electron microscopy of sheet silicates by computer simulation. *American Mineralogist*, 75, 276–288.

Hall A. (1999) Ammonium in granites and its petrogenetic significance. *Earth Science Review*, 45, 145–165.

Harlov D.E., Andrut M. & Poter B. (2001) Characterization of tobelite (NH_4) $Al_2(AlSi_3O_{10})OH_2$ and ND_4-tobelite ($ND_4)Al_2(Al_3Si_3O_{10})OH_2$ using IR spectroscopy and Rietveld refinement of XRD spectra. *Physics Chemistry Minerals*, 28, 268–276.

Higashi S. (1978) Dioctahedral mica minerals with ammonium ions. *Mineralogical Journal*, 9, 16–27.

Higashi S. (1982) Tobelite, a new ammonium dioctahedral mica. *Mineralogical Journal*, 11, 138–146.

Higashi S. (2000) Ammonium-bearing mica and mica/smectite of several pottery stone and pyrophyllite deposits in Japan: their mineralogical properties and utilization. *Applied Clay Science*, 16, 171–184.

Jackson M.L. (1975) *Soil Chemical Analysis – Advanced Course*. Published by author, Madison, WI, USA.

Jiang W.T., Essene E.J. & Peacor D.R. (1990a) Transmission electron microscopic study of coexisting pyrophyllite and muscovite: direct evidence for the metastability of illite. *Clays and Clay Minerals*, 38, 225–240.

Jiang W.T., Peacor D.R., Merriman R.J. & Roberts B. (1990b) Transmission and analytical electron microscopic study of mixed-layer illite/smectite formed as an apparent replacement product of diagenetic illite. *Clays and Clay Minerals*, 38, 449–468.

Jiang W.T. & Peacor D.R. (1993) Transmission and analytic electron microscopic study of mixed-layer illite/smectite formed as an apparent replacement product of diagenetic illite. *Clays and Clay Minerals*, 38, 449–468.

Juster T.C., Browne P.E. & Bailey S.W. (1987) NH_4-bearing illite in very low grade metamorphic rocks associated with coal, northeastern Pennsylvania. *American Mineralogist*, 72, 555–565.

Li G., Peacor D.R., Merriman R.J. & Roberts B. (1994) The diagenetic to low-grade metamorphic evolution of matrix white micas in the system muscovite-paragonite in a mudrock from Central Wales, United Kingdom. *Clays and Clay Minerals*, 42, 369–381.

Lindgreen H. (1994) Ammonium fixation during illite-smectite diagenesis in upper Jurassic shale North-Sea. *Clay Minerals*, 29, 527–537.

Lindgreen H., Drits V.A., Sakharov B.A., Salyn A. L., Wrang P. & Dainyak L.G. (2000) Illite-smectite structural changes during metamorphism in black Cambrian Alum shales from the Baltic area. *American Mineralogist*, 85, 1223–1238.

Livi K.J.T., Veblen D.R., Ferry J.M. & Frey M. (1997) Evolution of 2:1 layered silicates in low-grade metamorphosed Liassic shales of central Switzerland. *Journal of Metamorphic Geology*, **15**, 323–344.

Livi K.J.T., Christidis G.E., Árkai P. & Veblen D. (2008) White mica domain formation: a model for paragonite, margarite, and muscovite formation during prograde metamorphism. *American Mineralogist*, **93**, 520–527.

Marty B. (1995) Nitrogen content of the mantle inferred from N_2–Ar correlation in oceanic basalts. *Nature*, **377**, 326–329.

McHardy W.J. & Birnie A.C. (1987) Scanning electron microscopy. Pp. 74–208 in: *A Handbook of Determinative Methods in Clay Mineralogy* (M.J. Wilson, editor). Blackie, London, UK.

Mason P.R.D., Downes H., Thirlwall M.F., Seghedi I., Szakacs A., Lowry D. & Mattey D. (1996) Crustal assimilation as a major petrogenetic process in the East Carpathian Neogene and Quaternary margin arc, Romania. *Journal of Petrology*, **37**, 927–959.

Mason P.R.D., Seghedi I., Szakacs A. & Downes H. (1998) Magmatic constraints on geodynamic models of subduction in the East Carpathians. *Tectonophysics*, **297**, 157–176.

Moore D.M. & Reynolds R.C. (1997) *X-Ray Diffraction and the Identification and Analysis of Clay Minerals.* Oxford University Press, New York, NY, USA.

Nadeau P.H. & Bain D.C. (1986) Composition of some smectites and diagenetic illitic clays and implications for their origin. *Clays and Clay Minerals*, **34**, 455–463.

Nieto F. (2002) Tobelite in low-grade metamorphic organic-rich shales from Douro-Beira, Portugal. *American Mineralogist*, **87**, 205–216.

Nieto F., Ortega-Huertas M., Peacor D.R. & Arostegui J. (1996) Evolution of illite/smectite from early diagenesis through incipient metamorphism in sediments of the Basque-Cantabrian basin. *Clays and Clay Minerals*, **44**, 304–323.

Nieto F., Mellini M. & Abad I. (2010) The role of H_3O^+ in the crystal structure of illite. *Clays and Clay Minerals*, **58**, 238–246.

Peltz S., Vâjdea E., Balogh K. & Pécskay Z. (1987) Contributions to the chronological study of the volcanic processes in the Călimani and Harghita Mountains (East Carpathians, Romania). *Compte Rendu de Institute de Geologie e Geofisique*, **72–73**, 323–338.

Petit S., Righi D. & Madejová J. (2006) Infrared spectroscopy of NH_4^+-bearing and saturated clay minerals: a review of the study of layer charge. *Applied Clay Science*, **34**, 22–30.

Petschick R. (2000) *MacDiff.* Available at: http://www.ccp14.ac.uk/ccp/ccp14/ftp-mirror/krumm/Software/macintosh/macdiff/MacDiff.html.

Pöter B., Gottschalk M. & Heinrich W. (2007) Crystal-chemistry of synthetic K-feldspar-buddingtonite and muscovite-tobelite solid solutions. *American Mineralogist*, **92**, 151–165.

Reynolds R.C. (1985) *NEWMOD, a Computer Program for the Calculation of One Dimensional Diffraction Patterns of Mixed Layered Clays.* Hanover, NH, USA.

Ruiz-Cruz M.D. & Sanz de Galdeano C. (2008) Factors controlling the evolution of mineral assemblages and illite crystallinity in Paleozoic to Triassic sequences from the transition between Maláguide and Alpujáride complexes (Betic Cordillera, Spain): the significance of tobelite. *Clays and Clay Minerals*, **58**, 558–572.

Ruiz-Cruz M.D. & Sanz de Galdeano C. (2010) High-temperature ammonium white mica from the Betic Cordillera (Spain). *American Mineralogist*, **93**, 977–987.

Sakharov B.A., Lindgreen H., Salyn A. & Drits V.A. (1999) Determination of illite-smectite structures using multispecimen X-ray diffraction profile fitting. *Clays and Clay Minerals*, **47**, 555–566.

Schroeder P.A. & McLain A.A. (1998) Illite-smectite and the influence of burial diagenesis on the geochemical cycling of nitrogen. *Clay Minerals*, **33**, 539–546.

Szakacs A. & Seghedi I. (1995) The Călimani–Gurghiu–Harghita volcanic chain, Eastern Carpathians, Romania: volcanological features. *Acta Vulcanologica*, **7**, 145–153.

Seghedi I. & Downes H. (2011) Geochemistry and tectonic development of Cenozoic magmatism in the Carpathian–Pannonian region. *Gondwana Research*, **20**, 655–672.

Seghedi I., Balintoni I. & Szakacs A. (1998) Interplay of tectonics and Neogene post-collisional magmatism in the intracarpathian area. *Lithos*, **45**, 483–499.

Seghedi I., Downes H., Szakacs A., Mason P.R.D., Thirlwall M.F., Rosu E., Pécskay Z., Márton E. & Panaiotu C. (2004) Neogene–Quaternary magmatism and geodynamics in the Carpathian–Pannonian region: a synthesis. *Lithos*, **72**, 117–146.

Shau H.Y., Feather M.E., Essene E.J. & Peacor D.J. (1991) Genesis and solvus relations of submicroscopically intergrown paragonite and phengite in a blueschist from northern California. *Contribution to Mineralogy and Petrology*, **106**, 367–375.

Stanciu C. (1984) Hypogene alteration of Neogene volcanism of the East Carpathians. *Annuare de Institute de Geologique e Geofisique*, **LXIV**, 182–193.

Sterne E.J., Reynolds R.C. & Zantop H. (1982) Natural ammonium illites from black shales hosting a stratiform base metal deposit, Delong Mountains, Northern Alaska. *Clays and Clay Minerals*, **30**, 161–166.

Stevenson F.J. & Dharival A.P.S. (1959) Distribution of fixed ammonium in soil. *Soil Science of America Proceedings*, **23**, 121–125.

Šucha V., Kraus I. & Madejova J. (1994) Ammonium illite from anchimetamorphic shales associated with anthracite in the Zemplinicum of the Western Carpathians. *Clay Minerals*, **29**, 369–377.

Van der Pluijm B.A., Lee J.H. & Peacor D.R. (1988) Analytical electron microscopy and the problem of potassium diffusion. *Clays and Clay Minerals*, **36**, 498–504.

Veblen D.R., Guthrie G.D., Livi K.J.T. & Reynolds R.C. (1990) High-resolution transmission electron microscopy and electron diffraction of mixed-layer illite/smectite. *Clays and Clay Minerals*, **38**, 1–13.

Watenphul A., Wunder B. & Heinrich W. (2009) High-pressure ammonium-bearing silicates: implications for nitrogen and hydrogen storage in the Earth's mantle. *American Mineralogist*, **94**, 283–292.

Williams L.B. & Ferrell R.E. (1991) Ammonium substitution in illite during maturation of organic matter. *Clays and Clay Minerals*, **39**, 400–408.

Yau Y.C., Peacor D.R., Beans R.E., Essene E.J. & McDowell S.D. (1988) Microstructures, formation mechanisms, and the depth-zoning of phyllosilicates in geothermally altered shales, Salton Sea, California. *Clays and Clay Minerals*, **36**, 1–10.